

# *crystalAligner*: a computer program to align crystal directions in a scanning electron microscope by global optimization

Frank Niessen\*

Electron Microscopy Centre, University of Wollongong, Northfields Avenue, Wollongong, NSW 2522, Australia.

\*Correspondence e-mail: [contact@fniessen.com](mailto:contact@fniessen.com)

Received 6 August 2019

Accepted 30 December 2019

Edited by G. Kosterz, ETH Zurich, Switzerland

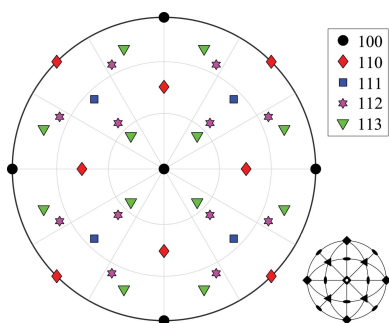
**Keywords:** scanning electron microscopy; electron backscatter diffraction; optimization.

Alignment of a crystal with the coordinate system of a scanning electron microscope (SEM) is essential for obtaining controlled diffraction conditions or investigating anisotropic material properties. The computer program *crystalAligner* was developed to enable the weighted constrained alignment of one or two crystal directions in crystals of arbitrary orientation and structure with the coordinate system of a SEM. For a given set of crystal directions, alignment objectives and rotational constraints, the algorithm simulates the rotation of the crystal on any constrained SEM stage and minimizes the misalignment of the crystal directions with prescribed coordinate axes of the SEM. The possibility of applying crystal symmetry and the use of a genetic algorithm for optimization ensure the determination of the global optimal alignment even in severely constrained conditions. In cases where ideal alignment is not obtainable, weighting factors can be applied to conflicting alignment objectives. Two application examples, the alignment of two crystal directions for a lamella lift out for nano-mechanical testing and the rotation of an orientation-related dual-phase microstructure into a standard projection, demonstrate the functionality and workflow of the freely available open-source program *crystalAligner*.

## 1. Introduction

Most metals, rocks and ceramics are polycrystalline under ambient conditions. The crystal structure describes the ordered arrangement of atoms and is characterized by symmetry elements. The symmetric arrangement of crystals is fully described by 230 space groups, which can be subdivided into 32 point groups (Noyan & Cohen, 1987). An essential implication of a crystal's lack of rotational symmetry is anisotropy of physical properties. Some well known physical properties that are subject to anisotropy are elasticity (anisotropy of Young's modulus) (Dölle, 1979; Ungár *et al.*, 1999), plasticity (*i.e.* anisotropy of slip system activity) (Oddershede *et al.*, 2015; Clausen *et al.*, 1998), the refractive index (Skalwold *et al.*, 2015; Quirke & Lacy, 1939) and magnetic susceptibility (Krishnan & Raman, 1927; Uyeda *et al.*, 1963). While the effects of anisotropy attenuate when approaching a uniform texture in a polycrystal, they must be considered in polycrystals with distinct texture or in single crystals (Kocks *et al.*, 2000).

Anisotropy plays an important role in imaging with electron microscopy. The contrast obtained from detecting back-scattered electrons in a scanning electron microscope (SEM) is dominated by the atomic number of the atoms in the probed volume. In addition to this contrast, the intensity of back-scattered electrons originating from crystalline materials is affected by the lattice spacing and the orientation of the



crystal lattice with respect to the axis of the primary beam. This contrast is known as electron channelling contrast and is closely related to diffraction contrast in a transmission electron microscope (TEM) (Zaefferer & Elhami, 2014; Borrajo-Pelaez & Hedström, 2018).

Both obtaining controlled diffraction conditions and investigating anisotropic effects in a SEM require knowledge of the orientation of a crystal and the ability to rotate this crystal towards a prescribed alignment with the SEM coordinate system. As TEM lamellae nowadays are commonly prepared in focused ion beam (FIB) equipped SEMs (Gianuzzi *et al.*, 1998), crystal alignment in the SEM is also useful for pre-aligning samples for analysis in the TEM.

Procedures of aligning a crystal with an external coordinate system have been established to obtain suitable diffraction conditions (two-beam conditions) for electron channelling contrast imaging (ECCI) (Gutierrez-Urrutia *et al.*, 2009; Mansour *et al.*, 2014; Zaefferer & Elhami, 2014). In the studies by Gutierrez-Urrutia *et al.* (2009) and Zaefferer & Elhami (2014) a crystal was aligned with the help of a computer program (Zaefferer, 2000) and crystal orientation data obtained from electron backscatter diffraction (EBSD). Mansour *et al.* (2014) computed similar manipulations based on orientation data from high-resolution selected area channelling patterns, which are claimed to allow orientation determination at higher angular resolution than obtained from Kikuchi patterns in EBSD.

While these examples are primarily focused on alignment of one crystal direction with the microscope coordinate system at maximum accuracy, analysis of anisotropic parameters often prioritizes the alignment of two crystal directions. Examples are the alignment of a bi-crystal for micro-compression testing (Kirchlechner *et al.*, 2017) and micro-mechanical testing of a single crystal along a specific crystal direction under controlled diffraction conditions (Ye *et al.*, 2010; Yu *et al.*, 2010). The alignment of two crystal directions is severely constrained when using common microscope stages with only two rotational degrees of freedom, one of which is restricted in range.

The developed program *crystalAligner* (Niessen, 2019b) enables alignment of one or two crystal directions in crystals of arbitrary orientation and structure with the coordinate system of the SEM by weighted multiobjective constrained optimization. Multiobjective optimization of the crystal alignment is tailored to work even on a standard SEM stage, which is commonly constrained to only two rotational axes and finite rotational limits. Efficient optimization of the alignment is realized by consideration of all symmetrically equivalent crystal directions and application of a genetic algorithm for determination of the global optimal alignment. Where applicable, multiple groups of equivalent crystal directions can be assigned to a single alignment objective which broadens the solution space to enable precise alignment under constrained conditions. In cases where a single solution cannot optimize both alignment objectives, a trade-off decision can be made either manually or by an automated multi-objective decision-making algorithm under consideration of objective weights.

The program was developed in MATLAB (MathWorks, 2016a) and makes use of basic functionalities of the crystallographic texture analysis toolbox *MTEX* (Bachmann *et al.*, 2010), ensuring an accurate and comprehensive description of crystal structures and symmetries, precise orientation visualization, and seamless integration into existing orientation analysis procedures. The first of two application examples demonstrates the alignment of two crystal directions of a crystal orientation determined with EBSD with the microscope coordinate system. After alignment, a TEM lamella is lifted out from this crystal for *in situ* nanomechanical testing in the TEM, where the prescribed crystal directions are aligned with the deformation axis and the axis of the electron beam to enable diffraction analysis. A second application example demonstrates the use of *crystalAligner* for rotating an orientation-related dual-phase microstructure into a standard projection for further analysis.

## 2. Theory

### 2.1. Hierarchy of coordinate systems

The alignment of prescribed crystal directions with the coordinate system of the electron microscope requires the definition of several hierarchical coordinate systems and their rotational relationships. The different coordinate axes and their rotational relationships are depicted in Fig. 1. In a polycrystal, the most local coordinate system is the crystal coordinate system,  $C_c$ , which has a defined alignment with the lattice vectors **a**, **b** and **c** of the unit cell. The rotational relationship between  $C_c$  and the coordinate system of the sample,  $C_s$ , is expressed by the Euler angles  $\phi_1$ ,  $\Phi$  and  $\phi_2$  (Bunge, 1982) and is more commonly termed the crystal orientation. In order

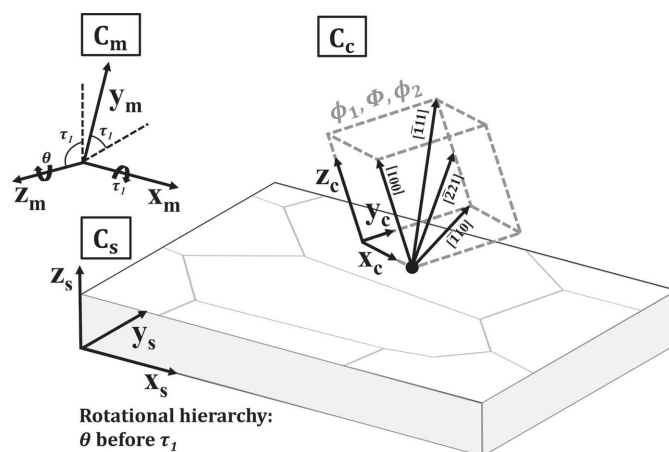


**Figure 1**  
Schematic of the definitions and rotational relationships of the hierarchical coordinate systems of the microscope ( $C_m$ ), the sample ( $C_s$ ) and the crystal ( $C_c$ ). The rotation of  $C_c$  around  $C_s$  is defined by Euler angles  $\phi_1$ ,  $\Phi$  and  $\phi_2$  and the rotation of  $C_s$  around  $C_m$  by the microscope stage rotations, here  $\theta$  and  $\tau_1$  around  $z_m$  and  $x_m$ , respectively. In a typical SEM stage layout, the axis hierarchy is tilt axis  $x_m$  over rotation axis  $z_m$ , i.e.  $C_s$  is rotated around  $z_m$  by  $\theta$  before it is tilted around  $x_m$  by  $\tau_1$ . The schematic shows a typical specimen tilt for EBSD analysis of  $\tau_1 = 70^\circ$  and  $C_c$  of a cubic crystal with examples of low-order crystal directions.

to align a crystal direction with the coordinate system of the microscope, any misalignment between the characteristic sample directions and the stage coordinate system must be known and considered during orientation determination and sample alignment.

The sample coordinate system  $C_s$  is related to the global coordinate system of the microscope chamber  $C_m$  by the rotational axes of the microscope stage. Common SEM stages enable unlimited rotation around  $z_m$  and limited tilt around either  $x_m$  or  $y_m$ . Advanced SEM stages or additional sub-stages may allow further rotational degrees of freedom.

## 2.2. Simulation of rotations

Optimization of the alignment of crystal directions with the microscope coordinate system  $C_m$  requires the simulation of the rotational relationships of the three hierarchical coordinate systems  $C_c$ ,  $C_s$  and  $C_m$ .

A crystal direction,  $\mathbf{h}_c^{uvw}$ , in the crystal coordinate system  $C_c$  may be defined by the Miller indices  $u$ ,  $v$  and  $w$ . (The chosen notation concerns the Miller notation of crystal directions  $uvw$ , but it is equally valid for the Miller notation of crystal plane normals  $hkl$  and the Bravais–Miller notation.) Crystal symmetry gives rise to  $n$  equivalent crystal directions  $(\mathbf{h}_c^{uvw})_n$ , which are obtained by multiplying the  $n$  characteristic symmetry matrices  $S_n$  (Engler & Randle, 2010) of a given point group with the normalized crystal direction  $\mathbf{h}_c^{uvw}$ :

$$(\mathbf{h}_c^{uvw})_n = S_n \mathbf{h}_c^{uvw}. \quad (1)$$

Fig. 2 shows a stereographic standard projection of some common low-order crystal directions in a cubic crystal (point group  $m\bar{3}m$ ) with all  $n = 24$  symmetry operations applied.

The rotational relationship of the crystal coordinate system  $C_c$  with respect to the sample coordinate system  $C_s$ , i.e. the

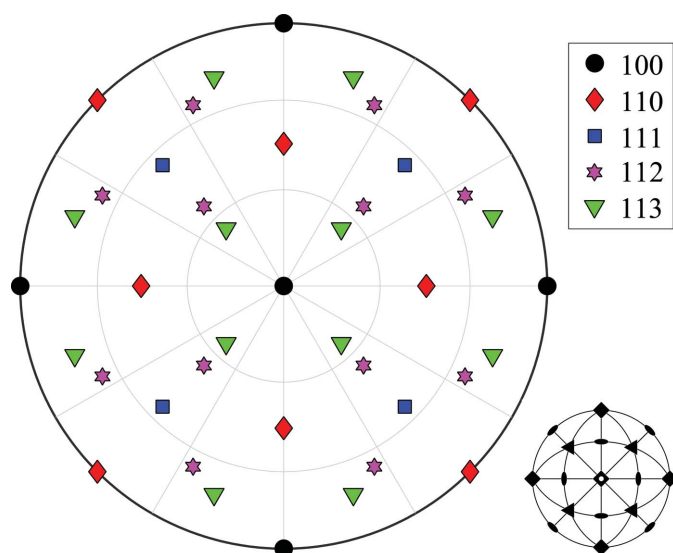


**Figure 2**  
Stereographic standard projection of the {100}, {110}, {111}, {112} and {113} equivalent crystal directions of a cubic crystal. The crystal symmetry of point group  $m\bar{3}m$  is indicated by the stereographic projection in the lower right corner.

crystal orientation, is denoted  $R_c^s$  and is given by three independent rotations following the Bunge notation (Bunge, 1982):

$$R_c^s = R_{\phi_2}^{z_s} R_{\Phi}^{x_s} R_{\phi_1}^{z_s}, \quad (2)$$

where  $\phi_1$ ,  $\Phi$  and  $\phi_2$  are the Euler angles.  $R_c^s$  consists of the three consecutive rotations of  $\phi_1$  around  $z_s$ ,  $\Phi$  around the new  $x_s$  and  $\phi_2$  around the new  $z_s$ . The crystal orientation in Euler angles is commonly determined with electron diffraction techniques, most prominently with EBSD (Humphreys, 2001).

The equivalent crystal directions  $(\mathbf{h}_c^{uvw})_n$  are transferred from the crystal coordinate system  $C_c$  (cf. standard projection in Fig. 2) to the sample coordinate system  $C_s$  by multiplication with the crystal orientation  $R_c^s$ :

$$(\mathbf{h}_s^{uvw})_n = R_c^s (\mathbf{h}_c^{uvw})_n. \quad (3)$$

Finally, to express the equivalent crystal directions  $(\mathbf{h}_s^{uvw})_n$  with respect to the microscope coordinate system  $C_m$ , the rotational relationship between  $C_s$  and  $C_m$  is applied, which is defined by the rotation matrix  $R_s^m$ :

$$(\mathbf{h}_m^{uvw})_n = R_s^m (\mathbf{h}_s^{uvw})_n. \quad (4)$$

$R_s^m$  is a compound rotation that consists of a sequence of elementary rotations around the fixed axes of the microscope coordinate system. The composition of the elementary rotations around the microscope axes is found by right multiplying the successive  $n$  elementary rotations  $R_i$  in order of decreasing hierarchy:

$$R_s^m = \prod_{i=1}^n R_i. \quad (5)$$

In the example depicted in Fig. 1, the axis hierarchy is tilt axis  $x_m$  over rotation axis  $z_m$ , i.e. rotation around  $z_m$  leaves the tilt axis  $x_m$  invariant, while the inverse is not true. Applying equation (5) to this specific stage setup, the following compound rotation matrix  $R_s^m$  is obtained:

$$R_s^m = R_{\tau_1}^{x_m} R_{\theta}^{z_m}, \quad (6)$$

with

$$R_{\tau_1}^{x_m} = \begin{bmatrix} 1 & 0 & 0 \\ 0 & \cos \tau_1 & -\sin \tau_1 \\ 0 & \sin \tau_1 & \cos \tau_1 \end{bmatrix}$$

and

$$R_{\theta}^{z_m} = \begin{bmatrix} \cos \theta & -\sin \theta & 0 \\ \sin \theta & \cos \theta & 0 \\ 0 & 0 & 1 \end{bmatrix},$$

$\tau_1$  being the stage tilt angle and  $\theta$  the stage rotation angle. The combination of equations (1) to (4) yields a single expression for describing all equivalent crystal directions of  $\mathbf{h}_c^{uvw}$  with respect to the global microscope coordinate system  $C_m$  for a given crystal orientation  $R_c^s$  and stage rotation  $R_s^m$ :

$$(\mathbf{h}_m^{uvw})_n = R_s^m R_c^s (\mathbf{h}_c^{uvw})_n = R_s^m R_{\phi_2}^{z_s} R_{\Phi}^{x_s} R_{\phi_1}^{z_s} S_n \mathbf{h}_c^{uvw}. \quad (7)$$

### 2.3. Alignment by multiobjective constrained optimization

Inspection of equation (7) shows that for a given crystal orientation  $R_c^s$  and crystal direction  $\mathbf{h}_c^{uvw}$  the microscope stage can be rotated and tilted to bring the crystal direction  $\mathbf{h}_c^{uvw}$  into alignment with an arbitrary axis of the global microscope coordinate system  $C_m$ . Optimization of this alignment is, in reality, limited by the number and reach of the rotational axes of the SEM stage. Default SEM stages have only two rotational degrees of freedom: unlimited rotation around  $z_m$  and tilt by at least  $-5$  to  $60^\circ$  around either  $x_m$  or  $y_m$ . More recent instruments cover a significantly wider tilt range of up to  $-90$  to  $90^\circ$ . Such strict rotational constraints of a standard SEM stage might very well be able to give a sufficiently broad solution space when aligning a single equivalent crystal direction of a highly symmetric crystal structure. The same rotational constraints may, however, limit the alignment of two equivalent crystal directions of a low-symmetry crystal structure. In such cases, multiobjective optimization algorithms can be applied to find a group of feasible trade-off solutions to the alignment problem.

The absolute angular deviation from perfect parallel alignment,  $\varepsilon_m$ , between the most favourable of all evaluated equivalent crystal directions  $(\mathbf{h}_m^{uvw})_n$  and a microscope coordinate axis  $\mathbf{c}_m$  is given by the minimum of all respective angular misalignments,  $\varepsilon_n$ :

$$\varepsilon_m = \min\{\varepsilon_n\} = \min\left\{\cos^{-1}\left[\frac{(\mathbf{h}_m^{uvw})_n \cdot \mathbf{c}_m}{|(\mathbf{h}_m^{uvw})_n||\mathbf{c}_m|}\right]\right\}. \quad (8)$$

Equation (8) is the objective function of the optimization problem. The number of objective functions and values for  $\varepsilon_m$  is equal to the number of objectives. In the terminology of the genetic algorithm applied here, equation (8) is a ‘fitness function’ and  $\varepsilon$  a ‘fitness function value’. The variables of the objective function are the stage tilt and rotation angles [cf. equations (6) and (7)] which are constrained by their upper and lower bounds, *i.e.* the hard or soft stage limits. The square of  $\varepsilon_m$  in equation (8) was also evaluated as a fitness function value, but it did not appear to improve the convergence or the stability of the optimization algorithm.

## 3. Description of the computer program

### 3.1. Program structure

The presented theory for alignment of a crystal with the coordinate system of a SEM was implemented in the computer program *crystalAligner*, written in MATLAB (MathWorks, 2016a). The program utilizes elements of the crystallographic texture analysis toolbox *MTEX* (Bachmann *et al.*, 2010) for the definition of crystal structures and symmetries, orientation visualization, and crystallographic calculations. Additionally, the single- and multiobjective genetic algorithm functions *ga* and *gamultiobj* of the MATLAB global optimization toolbox (MathWorks, 2016b) for optimization of the crystal alignment are applied. The basic structure of the program is summarized in the flow chart in Fig. 3.

First, variables concerning the crystal structure, the experimentally determined crystal orientation and the equivalent crystal directions for alignment are declared and initialized. It is possible to assign individual alignment objectives to different crystals of arbitrary orientation and structure. Here, crystal symmetry can be activated or disregarded. Apart from the standard Miller notation, both the Miller and Miller–Bravais notations of hexagonal and rhombohedral crystal structures are supported for the specification of crystal directions and plane normals. Then, the rotational axes and limits of the microscope stage and the microscope axes for alignment are specified. The program structure allows the definition of any microscope stage with an arbitrary number and hierarchy of axes and hard or soft stage limits. Finally, optimization and post-processing parameters are indicated.

The initial crystal orientation and a stereographic projection of the specified equivalent crystal directions are plotted with respect to the microscope coordinate system  $C_m$  at no applied stage tilt and rotation. These plots serve to qualitatively assess whether satisfying crystal alignment is likely to be achieved for a given crystal orientation and structure within given constraints.

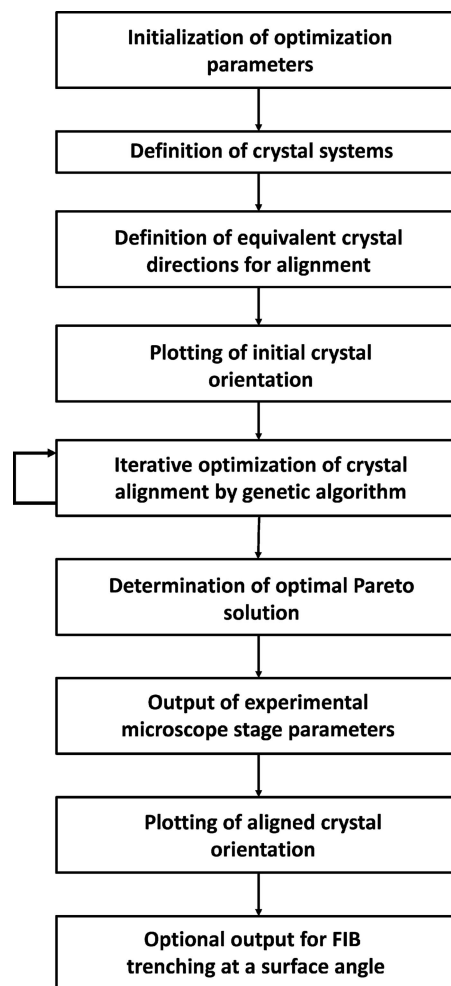


**Figure 3**  
Flow chart of the basic structure of the computer program *crystalAligner*.



The single- or multiobjective genetic algorithm is then set up with the fitness function in equation (8) and the specified optimization parameters. The alignment of specified crystal directions with the microscope coordinate system  $C_m$  is optimized iteratively by the genetic algorithm (see Section 3.2 for more details). The optimal experimental stage parameters are returned and the orientation of the crystal and a stereographic projection of the equivalent crystal directions with respect to the microscope coordinate system are plotted. When the specimen coordinate system is aligned with the microscope coordinate system, the determined axis rotations may be directly applied to the sample. In the case of a known misalignment of these coordinate systems (caused, for example, by applying a pre-tilt to the sample), the misalignment can either be accounted for manually or defined as a static stage axis. In the case of crystal alignment for preparation of an aligned lift out of a TEM lamella, optional output for adjustment of the trench sizes for a tilted sample surface are computed as well. A comprehensive user manual for the *crystalAligner* computer program including several application examples is provided by Niessen (2019b).

## 3.2. Constrained multiobjective minimization using the genetic algorithm

The genetic algorithm is a method that solves optimization problems based on the principles of natural selection. It iteratively finds the most suitable solutions for an optimization problem from a population of solutions and uses these as parents to form the next generation of solutions. The advantage of the genetic algorithm as a stochastic population-based algorithm, compared with solver-based optimization algorithms, is that it is more likely to find global rather than local minima. On the downside, the solution generated by the genetic algorithm depends to a certain degree on the initial population.

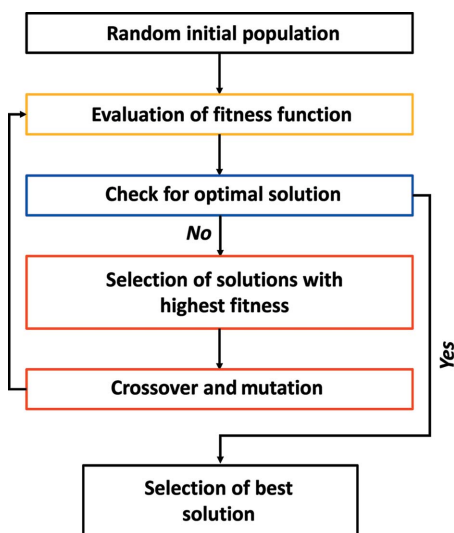


**Figure 4**  
Simplified flow chart of the main iteration of a genetic algorithm.

A simplified flow chart of the main iteration of the genetic algorithm is given in Fig. 4. The *ga* and *gamultiobj* functions of the MATLAB optimization toolbox (MathWorks, 2016b) are applied for single- and multiobjective optimization, respectively. In the following, more detail on the genetic algorithm method is provided; for a more in-depth treatment of the genetic algorithm, references Goldberg (1989) and MathWorks (2016c) are recommended.

In the present application, the input argument to the fitness function in equation (8) is the vector of active stage axis rotations. In the terminology of evolution, the vectors of variables applied to the fitness function are termed individuals, the variables are termed genes and the overall variable space is termed the population. The iterative optimization loop starts by evaluating the fitness function with the initial population. For each individual, fitness function values are returned which are termed raw scores.

Parents that form the next generation by crossover and mutation are selected on the basis of their fitness, which is derived from their raw scores. It is crucial to identify parents with high fitness without introducing bias towards specific solutions. In single-objective optimization selection, this is realized by stochastic universal sampling (Baker, 1987), and in multiobjective optimization, the selection process is carried out by tournament selection (Miller & Goldberg, 1995). In the present application, the next generation is formed by a balance of 5% of elite individuals that are guaranteed to survive, 80% of children from crossover by qualified individuals and 15% of mutation children. Only a well proportioned balance of elite, crossover and mutation leads to efficient convergence of the optimization problem (MathWorks, 2016c).

The next iterative loop commences by applying the new generation of individuals to the fitness function. In single-objective optimization the algorithm stops when the average change in fitness value is below a set function tolerance. In multiobjective optimization, the evolution of the solution space is analysed to identify convergence.

## 3.3. Multi-objective decision making

For multiobjective optimization of non-trivial problems, in general no solution can simultaneously optimize all objectives. The optimization algorithm provides a number of Pareto optimal solutions, *i.e.* solutions for which one fitness function value cannot be improved further without degrading some of the other fitness function values. In the case of two or three objectives, the Pareto optimal solutions can be visually compared by plotting the fitness function values of the Pareto optimal solutions against each other. These values form a 'Pareto front' around the origin, also known as a trade-off curve (see Fig. 7 in application example 1, Section 4). The multiobjective genetic algorithm stops if the spread, a measure of the movement of the Pareto front, is lower than a set function tolerance.

None of the Pareto optimal solutions is *per se* inferior to another. The optimal solution is application dependent and, as

**Table 1**

Experimental and optimization parameters for the alignment of two crystal directions with axes of the SEM coordinate system in application example 1.

Material properties	
Material	Near- $\beta$ Ti-10V-2Fe-3Al
Crystal structure	Body-centred cubic
Point group	$m\bar{3}m$
Electron backscatter diffraction on bulk sample	
Sample tilt angle ( $^{\circ}$ )	70
Working distance (mm)	8
Analysis area ( $\mu\text{m}$ )	$420 \times 290$
Discretization ( $\mu\text{m}$ )	5
Acquisition time (s)	184
Optimization problem	
Initial crystal orientation ( $^{\circ}$ )	$\phi_1 = 61, \Phi = 42, \phi_2 = 9$
Alignment objective 1	$\langle 113 \rangle \parallel y_m$
Alignment objective 2	$\langle 1\bar{1}0 \rangle \parallel z_m$
Stage rotation axes	$x_m$ and $z_m$
Rotational limits ( $^{\circ}$ )	$x_m: 0 < \tau_1 < 20$ $z_m: 0 < \theta < 360$
Multi-objective genetic algorithm	
Fitness function	Equation (8)
Function variables	Stage axis rotations $\tau_1$ and $\theta$
Bound constraints	Rotational limits
Population size	50
Function tolerance	0.01
Maximum stall generations	10
Weighting factors	$w_1 = 1$ and $w_2 = 1$
Multiobjective decision	TOPSIS method
Optimized crystal alignment	
Aligned crystal orientation ( $^{\circ}$ )	$\phi_1 = 196, \Phi = 35, \phi_2 = 6$
Stage axis rotations ( $^{\circ}$ )	$\tau_1 = 7.2$ and $\theta = 132.5$
Fitness values (deviation) ( $^{\circ}$ )	$\varepsilon_1 = 0.1$ and $\varepsilon_2 = 0.8$
Transmission Kikuchi diffraction on TEM lamella	
Sample tilt angle ( $^{\circ}$ )	-20
Working distance (mm)	3.9
Analysis area ( $\mu\text{m}$ )	$27.6 \times 12$
Discretization ( $\mu\text{m}$ )	0.3
Acquisition time (s)	492

a trade-off is inevitable, requires weighting of the objectives. In the program *crystalAligner*, the user is able to either manually choose the best solution from the Pareto optimal solutions or rely on the automated TOPSIS (technique for order of preference by similarity to ideal solution) decision-making method (Tseng & Huang, 2011). The TOPSIS method compares the fitness function values under consideration of weighted objectives with the best and worst alternatives for each objective. The comparison yields a score for each solution which enables ranking of the Pareto optimal solutions.

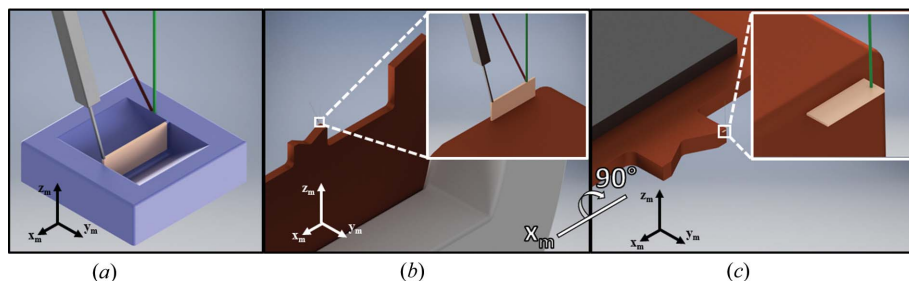
#### 4. Application example 1

The first application example demonstrates the workflow and functionality of the program *crystalAligner* and provides an example for a set of experimental and computational parameters. Two equivalent crystal directions,  $\langle 110 \rangle$  and  $\langle 113 \rangle$ , of a body-centred cubic crystal are simultaneously aligned with the SEM coordinate system to enable the lift out of an aligned TEM lamella. The TEM lamella is then used as the base material to machine samples for nano-tensile testing with a native  $\langle 113 \rangle$  zone axis and a  $\langle 110 \rangle$  tensile axis. The lift-out geometry is described, details about the investigated material and experimental setup are provided, the experimental and computational alignment procedures are outlined, and finally the resulting alignment is experimentally validated. A list of all experimental and optimization parameters is given in Table 1.

##### 4.1. Geometry of TEM lamella lift out

Fig. 5 shows the orientation of a TEM lamella during different steps of the preparation process with respect to the microscope coordinate system  $C_m$  of a FIB/SEM instrument. In particular, Fig. 5(a) shows the lift out of the lamella from the bulk, Fig. 5(b) shows the attachment of the lamella to the lift-out grid and Fig. 5(c) shows the final orientation of the lamella during imaging in the FIB/SEM instrument. The

electron beam (green) is oriented parallel to  $z_m$  and the ion beam (red) is tilted  $52^{\circ}$  around  $x_m$  with respect to the electron column. The stage rotations to align the crystal directions with EBSD are conventionally determined at a  $70^{\circ}$  stage tilt, and then a protective layer is deposited along the length of the lamella, conventionally at a  $0^{\circ}$  stage tilt. This stage orientation is termed the lift-out orientation and, in the particular case of aligning crystal directions with  $C_m$ , this stage orientation could be at a nonzero tilt angle. Next, the sample is tilted towards the ion beam for trenching and initial thinning, and it is then tilted back to the lift-out stage orientation. In the lift-out stage orientation, the electron beam is parallel to the

**Figure 5**

Schematic of the geometry of a TEM lamella lift out in a FIB/SEM instrument. The coordinate axes refer to coordinate system  $C_m$  and the green and red lines correspond to the electron and ion beam, respectively. (a) Lamella, formed by trenching and initial thinning with the FIB, attached to the micro-manipulator in the lift-out orientation. (b) Deposition of the lamella with the micro-manipulator on a TEM lift-out grid. (c) Thinned lamella during the final imaging stage in the FIB/SEM instrument. The electron beam is perpendicular to the thinned sample surface; this alignment between the sample and electron beam is equivalent to the initial alignment in a TEM. Between the preparation steps in (a) and (b) and the imaging step in (c), the lamella undergoes a rotation of  $90^{\circ}$  around  $x_m$ .

plane surface of the lamella [Fig. 5(a)]. The TEM lamella is cut off from the bulk sample and lifted out with a micro-manipulator parallel to the axis of the electron beam. The TEM lamella is then deposited on an upwards facing lift-out grid with its front facing parallel to the electron beam [Fig. 5(b)]. After thinning of the lamella with the ion beam oriented at grazing incidence to the lamella surface, the final imaging in the FIB/SEM instrument is carried out with the electron beam perpendicular to the thin electron-transparent direction of the TEM lamella [Fig. 5(c)]. This orientation of the lamella with respect to the electron beam is equivalent to the initial orientation with the electron beam in a TEM. From the lift out of the lamella [Fig. 5(a)] to the final imaging step [Fig. 5(c)], the lamella undergoes a  $90^\circ$  rotation around  $x_m$  [see rotation of the lift-out grid from Figs. 5(b) and 5(c)]. For *in situ* nano-tensile testing in the TEM, the lamella is required to have a  $\langle 113 \rangle$  native zone axis [parallel to  $z_m$  in Fig. 5(c)] and a  $\langle 110 \rangle$  tensile axis [parallel to  $y_m$  in Fig. 5(c)]. The rotation of the lamella by  $90^\circ$  around  $x_m$  during the preparation process thus requires an initial parallel alignment of  $\langle 113 \rangle$  with  $y_m$  and  $\langle 110 \rangle$  with  $z_m$  of the bulk crystal in Fig. 5(a).

#### 4.2. Material and experimental setup

The material subjected to nano-mechanical testing was a near- $\beta$  Ti–10V–2Fe–3Al (wt%) alloy. The sample was solution treated at 1123 K for 840 s to form the body-centred cubic  $\beta$  phase and, without cooling to room temperature, annealed at 973 K for 500 s to form  $\sim 5$  vol.% of the hexagonal closed-packed  $\alpha$  phase.

The preparation of the TEM lamella was carried out with an FEI Helios NanoLab G3 CX FIB/SEM instrument. The standard stage of the instrument has limitless rotation around  $z_m$  and tilt around  $x_m$  with hard limits of  $-15$  and  $90^\circ$ . EBSD crystal orientation measurements were conducted with an

Oxford Instruments NordlysMax3 high-speed EBSD camera. The crystal orientation as an input to *crystalAligner* was obtained from the online Oxford Instruments *Aztec* software (Oxford Instruments, 2016). All offline processing of EBSD data was conducted in *MTEX 5.1.1* (Bachmann *et al.*, 2010).

#### 4.3. Initial orientation measurement

The bulk sample was mounted with its surface plane parallel to the SEM stage. The initial value of the stage rotation  $\theta$  was redefined to  $0^\circ$ . The microscope was set up for EBSD analysis with parameters that enable fast and confident mapping of the orientation data of a few crystals (see parameters in Table 1).

The inverse pole figure (IPF) map from EBSD analysis of the microstructure of the bulk sample is shown in Fig. 6(a) with respect to  $C_s$  or the equivalent  $C_m$  at no stage tilt and rotation. Visual inspection of the IPF maps with respect to the  $y_m$  and  $z_m$  axes allows a preliminary selection of crystals that appear to lead to satisfactory alignment within the given rotational constraints. The  $\langle 113 \rangle$  direction of the encircled crystal in Fig. 6(a) appears to be in close proximity to  $y_m$  at no applied stage rotation and tilt, indicating good chances of ideal alignment with *crystalAligner*. The Euler angles of this crystal are therefore inserted into the computer program, which generates orientation figures to further access chances of ideal alignment. Fig. 6(b) shows IPFs of the crystal orientation with respect to the three coordinate axes of the microscope at  $0^\circ$  stage rotation and tilt (black round markers) in direct comparison with the two alignment objectives (white squared markers). Fig. 6(c) shows the stereographic projection of  $\langle 110 \rangle$  and  $\langle 113 \rangle$  of the crystal orientation with respect to  $C_m$  at  $0^\circ$  stage rotation and tilt in comparison with the alignment objectives (white markers). The orientation plots suggest that the crystal might be successfully aligned within the narrow rotational constraints of the microscope stage.

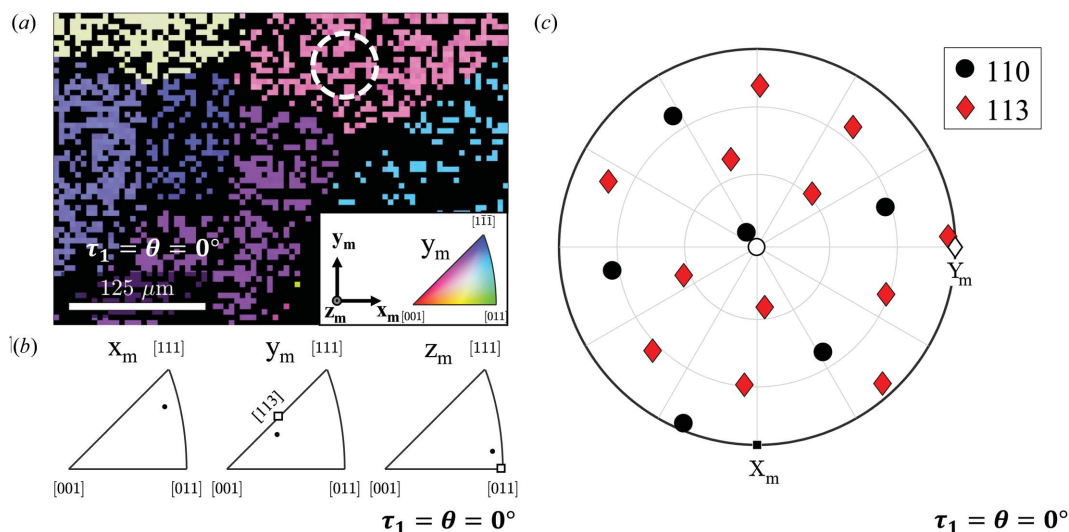


**Figure 6** Orientation data of the unaligned crystal with respect to the sample coordinate system  $C_s$  or the equivalent microscope coordinate system  $C_m$  at no stage tilt and rotation. (a) Inverse pole figure map of the  $\beta$ -phase bulk microstructure from EBSD analysis, showing the origin of the chosen crystal orientation for alignment (white circle). (b) Inverse pole figure of the crystal orientation (black round markers) compared with the alignment objectives (white square markers). (c) Stereographic projection of  $\langle 110 \rangle$  and  $\langle 113 \rangle$  compared with the alignment objectives (white markers).

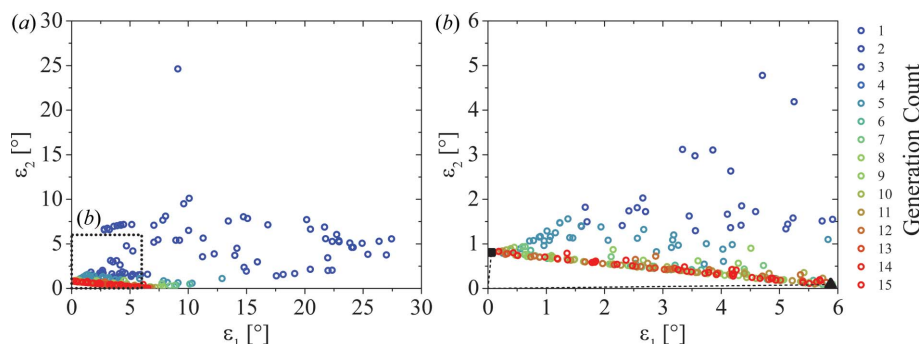


Figure 7

(a) Evolution of the feasible fitness function values [equation (8)] over the 15 colour-graded generations. (b) Enlargement of the inset to (a), showing the Pareto optimal solutions forming a Pareto front. The most attractive optimal Pareto solution in the present application was found with the TOPSIS method and is shown by the black square marker. For the purpose of demonstration, the black triangular marker shows the optimal solution obtained from the TOPSIS method when applying weighting factors  $w_2/w_1 = 10$ .

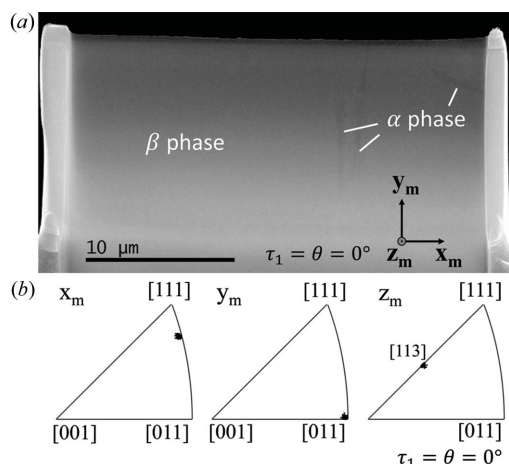


Figure 8

(a) Forward-scatter electron image of the thinned lamella, lifted out from the crystal in Fig. 6(a) after alignment with the microscope coordinate system. The lamella consists of  $\alpha$ -phase inclusions in a single  $\beta$ -phase grain. (b) Inverse pole figures from transmission Kikuchi diffraction analysis of the  $\beta$  phase of the thinned lamella with respect to the microscope coordinate axes shown in (a). The directions  $x_m$ ,  $y_m$  and  $z_m$  are shown in (a). Axes  $y_m$  and  $z_m$  were successfully aligned with  $\langle 011 \rangle$  and  $\langle 113 \rangle$ , respectively.

#### 4.4. Multiobjective constrained optimization

The alignment of the mutually perpendicular directions  $[110]$  and  $[\bar{1}13]$  with  $y_m$  and  $z_m$ , respectively, has a unique and unambiguous solution. The application of crystal symmetry extends the solution space to 24 possible solutions. The optimization problem concerns finding a solution with minimal misalignment to any of these 24 solutions without violating the linear rotational constraints of the SEM stage, which makes this a non-trivial optimization problem.

The initial crystal orientation of  $\phi_1 = 61^\circ$ ,  $\Phi = 42^\circ$ ,  $\phi_2 = 9^\circ$  with respect to  $C_m$  at  $0^\circ$  stage tilt and rotation is taken as an input argument to the optimization algorithm. Starting from a uniformly spread population of feasible solutions,<sup>1</sup> the algo-

rithm simulates and optimizes stage rotation and tilt with the objective of minimizing the misalignment between the two specified pairs of equivalent crystal directions and the supplied microscope axes according to the fitness function in equation (8). The applied alignment objectives, variables and bound constraints are summarized in Table 1. The limits of the tilt axis are intentionally constrained to the soft limits of 0 and  $20^\circ$  in the present optimization problem to allow additional tilting by  $52^\circ$  from the lift-out position for FIB trenching. A negative tilt range was avoided, as it would prohibit the insertion of the gas-injection system needle for deposition of a protective

layer in the SEM used.

After  $\sim 30$  s runtime on a standard contemporary office computer, the multiobjective genetic algorithm terminated the optimization procedure after 15 generations with an average change in the spread of Pareto solutions below the specified function tolerance.

Fig. 7(a) shows a plot of the evolution of the feasible fitness function values  $\varepsilon_1$  and  $\varepsilon_2$  over the course of 15 generations, represented in ascending order with the colour transition from blue to red. The fitness function values correspond to the absolute angular deviation from perfect alignment for objectives 1 and 2, respectively. It is evident that new generations successfully optimize the two alignment objectives. Fig. 7(b) shows a magnified inset of Fig. 7(a) to highlight the distribution of the final fitness function values. With increasing generation count, the fitness function values approach the origin, which represents ideal fulfilment of both alignment objectives. The fitness function values of the Pareto optimal solutions form a clearly distinct front, which is termed the 'Pareto front' or trade-off curve. The Pareto optimal solutions all represent optimal solutions with different trade-offs. The TOPSIS method for automated multiobjective decision making (*cf.* Section 3.3) determined an optimal stage tilt and rotation of  $\tau_1 = 7.2^\circ$  and  $\theta = 132.5^\circ$ , respectively, with absolute angular deviations from ideal alignment of  $\varepsilon_1 = 0.1^\circ$  and  $\varepsilon_2 = 0.8^\circ$ , respectively [black square marker in Fig. 7(b)]. For the purpose of demonstrating the application of the TOPSIS method with weighted objectives, the two alignment objectives were weighted with  $w_1 = 1$  and  $w_2 = 10$ , leading to optimal tilt  $\tau_1 = 7.2^\circ$  and rotation  $\theta = 126.6^\circ$  with absolute angular deviations from ideal alignment of  $\varepsilon_1 = 5.9^\circ$  and  $\varepsilon_2 = 0.1^\circ$  [black triangular marker in Fig. 7(b)].

#### 4.5. TEM lamella preparation at an inclined surface

A TEM lamella was prepared according to the procedure shown in Fig. 5. The lamella lift out [Fig. 5(a)] was conducted at the optimized stage tilt  $\tau_1 = 7.2^\circ$  and rotation  $\theta = 132.5^\circ$ . For trenching, the tilt was increased by  $52^\circ$ , the angle between the

<sup>1</sup> Fitness function values are feasible if they satisfy the given constraints.



SEM and FIB column, resulting in  $\tau_1 = 59.2^\circ$ . The maximum achievable tilt angle is instrument dependent and limited by the pole piece geometry, the eucentric height and the stage limit of the used FIB/SEM instrument as well as the sample geometry. A straightforward method of extending the tilt range for a TEM lamella lift out is the application of an additional rotation of the sample by  $180^\circ$ . This operation then leads to a symmetrically equivalent alignment at the lift-out position for a stage tilt of  $\tau_1 = -7.2^\circ$  instead of  $7.2^\circ$ . The additional stage rotation thus reduces the stage tilt in the trenching position to  $\tau_1 = -7.2^\circ + 52^\circ = 44.8^\circ$ .

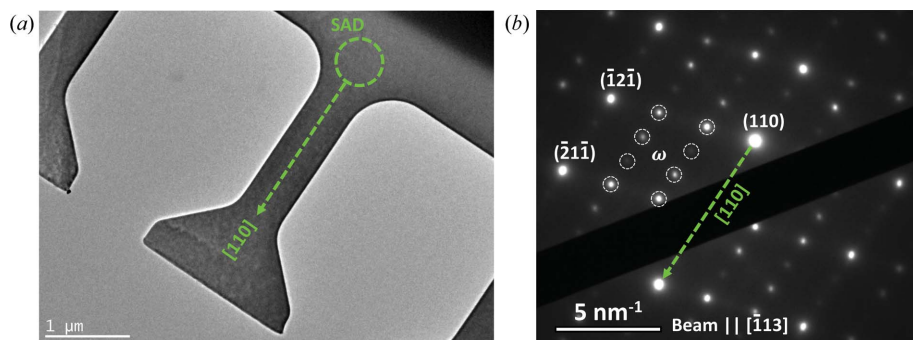
Since the surface of the sample is inclined by  $7.2^\circ$  compared with a conventional lift out, the optimal sizes of the trenches on either side of the lamella are not equal as is usually the case for a conventional lift out [Fig. 5(a)]. With computation of the optimal stage rotations for crystal alignment, the *crystalAligner* program optionally assists in calculating the ideal

trench sizes for lift outs of TEM lamellae at an inclined surface.

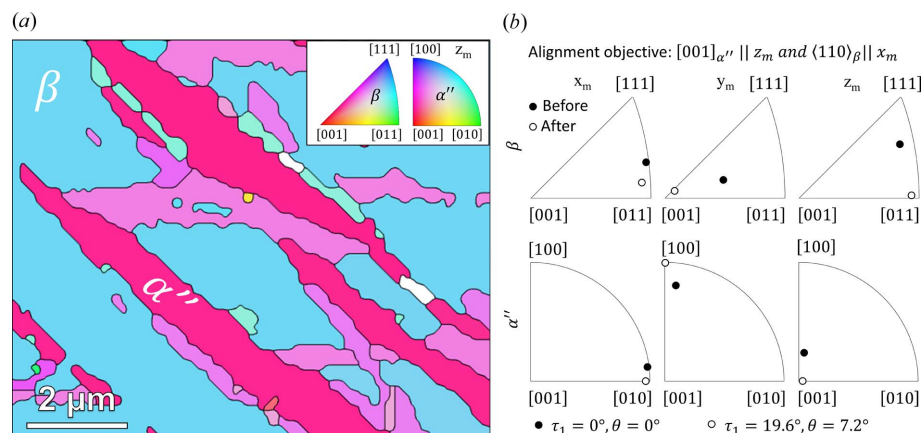
## 4.6. Experimental validation

Fig. 8(a) shows the TEM lamella after thinning in the orientation shown in Fig. 5(c). The lamella consists of a single  $\beta$ -phase matrix with a few  $\alpha$ -phase inclusions (dark elongated grains). The IPFs of the  $\beta$  phase in Fig. 8(b) were determined with transmission Kikuchi diffraction (parameters listed in Table 1). It is apparent that the respective alignment of the microscope coordinate axes  $y_m$  and  $z_m$  with  $\langle 011 \rangle$  and  $\langle 113 \rangle$  was successful.

After thinning of the lamella, samples for nano-scale *in situ* tensile testing were machined by FIB milling with computer-designed machining patterns prepared with the open-source software *CAM2FIB* (Niessen, 2019a; Niessen & Nancarrow, 2019). Fig. 9 shows one of these tensile samples in a TEM bright-field image with its selected area electron diffraction pattern at no applied sample tilt. The diffraction pattern was taken along the  $[\bar{1}13]$  zone axis. Identification of the  $[110]$  direction in the diffraction pattern and transferring it to the bright-field image proves that the tensile axis was successfully aligned with  $[110]$ . The additional spots in the diffraction pattern indicate the presence of nano-scale athermal  $\omega$  particles, which form upon quenching from the annealing temperature and cannot be resolved with EBSD analysis or conventional SEM imaging techniques (Naseri *et al.*, 2019).



**Figure 9**  
(a) TEM bright-field image of a sample machined for nano-tension testing at  $0^\circ$  sample tilt. The  $[110]$  axis is parallel to the tensile axis of the sample. (b) Selected area electron diffraction pattern of the  $\beta$  and  $\omega$  phases. The applied crystal alignment before lifting out the lamella enabled parallel alignment of the  $[110]$  crystal direction of the  $\beta$  phase with the deformation axis (green broken arrow) and the  $[113]$  direction of the  $\beta$  phase with the electron beam. The reflections that reveal the existence of the athermal  $\omega$  phase are highlighted by white circles.



**Figure 10**  
(a) Thermally induced  $\alpha'$  martensite in a single-orientation  $\beta$  matrix (blue crystals) of a near- $\beta$  Ti–10V–2Fe–3Al alloy. The two marked crystals are aligned according to the objectives listed in Table 2. (b) Inverse pole figures of  $\alpha'$  and  $\beta$  with reference to the microscope coordinate axes  $x_m$ ,  $y_m$  and  $z_m$  and the stage tilt and rotation angles  $\tau_1$  and  $\theta$ . It is evident that the alignment rotates the initial orientation (black markers) into the  $\alpha'$  cube orientation (white markers).

## 5. Application example 2

The second application example demonstrates the rotation of two phases of a  $\beta$  titanium deformation microstructure with a known orientation relationship into a standard cube projection. The sample and heat treatment are identical to those in application example 1 (Table 1). Depending on the stability of the  $\beta$  phase in near- $\beta$  Ti alloys and the local quench rate, the  $\beta$  phase may partially transform to  $\alpha'$  martensite during quenching from the annealing treatment by a displacive phase transformation.  $\alpha'$  martensite has an orthorhombic crystal structure (point group  $mmm$ ) and maintains the following orientation relationship with the  $\beta$  phase (Chai *et al.*, 2009):

**Table 2**

Experimental and optimization parameters for the alignment of two crystal directions with axes of the SEM coordinate system in the second application example (Section 5).

Optimization problem	
Initial crystal orientations (°)	$\beta$ : $\phi_1 = 261$ , $\Phi = 43$ , $\phi_2 = 28$ $\alpha''$ : $\phi_1 = 175$ , $\Phi = 20$ , $\phi_2 = 102$
Alignment objective 1	$\langle 110 \rangle_\beta \parallel x_m$
Alignment objective 2	$[001]_{\alpha''} \parallel z_m$
Stage rotation axes	$x_m$ and $z_m$
Rotational limits (°)	$x_m$ : $0 < \tau_1 < 20$ $z_m$ : $0 < \theta < 360$
Multiobjective genetic algorithm	
Fitness function	Equation (8)
Function variables	Stage axis rotations $\tau_1$ and $\theta$
Bound constraints	Rotational limits
Population size	500
Function tolerance	0.01
Maximum stall generations	10
Weighting factors	$w_1 = 1$ and $w_2 = 1$
Multiobjective decision	TOPSIS method
Optimized crystal alignment	
Aligned crystal orientation (°)	$\beta$ : $\phi_1 = 276$ , $\Phi = 41$ , $\phi_2 = 359$ $\alpha''$ : $\phi_1 = 90$ , $\Phi = 4$ , $\phi_2 = 180$
Stage axis rotations (°)	$\tau_1 = 19.6$ and $\theta = -6.9$
Fitness values (deviation) (°)	$\varepsilon_1 = 6.3$ and $\varepsilon_2 = 4.0$

$$\text{OR}^{\text{theo}} = \begin{bmatrix} [100]_{\alpha''} \parallel [100]_\beta \\ [010]_{\alpha''} \parallel [011]_\beta \\ [001]_{\alpha''} \parallel [0\bar{1}1]_\beta \end{bmatrix}.$$

There are six different variants that can be derived from the  $\langle 100 \rangle_\beta$ ,  $\langle 011 \rangle_{z_m}$  and  $\langle 0\bar{1}1 \rangle_\beta$  orientations in the  $\beta$  crystal (Chai *et al.*, 2009). Fig. 10(a) shows a local EBSD orientation map of a  $\beta$  and  $\alpha''$  microstructure. The map shows a single  $\beta$  orientation and differently oriented  $\alpha''$  variants. The marked variant does not deviate significantly from a cube orientation, which makes it favourable for rotation into its standard projection. In order to bring the microstructure into the  $\alpha''$  cube standard projection employed in the definition of the orientation relationship,  $[001]_{\alpha''}$  is aligned parallel to  $z_m$  and any of the  $\langle 110 \rangle_\beta$  equivalent directions is aligned parallel to  $x_m$ . According to the above-stated orientation relationship between  $\alpha''$  and  $\beta$ , the second alignment objective could alternatively be defined as  $[010]_{\alpha''}$  parallel to  $x_m$ ; this was omitted in the present case to demonstrate the functionality of the computer program of defining multiple alignment objectives in dissimilar crystals. The parameters used for the alignment procedure are given in Table 2. In contrast to the first application example, the crystal alignment in the present example concerns the orthorhombic crystal structure, which, due its low symmetry, drastically reduces the number of possible solutions to the objective function. The narrowed solution space must be accounted for by increasing the population size in the genetic optimization algorithm to avoid running into local optima. Furthermore, a suitable initial orientation is essential for successful alignment and a larger misalignment error must be accepted.

The aligned crystal orientations are given in Table 2 and are plotted in Fig. 10(b). It was possible to rotate the orientation relationship into a cube projection with 6.3° misalignment

**Table 3**

Descriptive statistics on the accumulated optimal fitness function value  $\varepsilon$  from 1000 executions of the first application example in Section 4 for assessing the robustness of the genetic algorithm.

Population size	50	100
Mean $\varepsilon$ (°)	1.032	0.872
Median $\varepsilon$ (°)	0.872	0.816
Minimum $\varepsilon$ (°)	0.801	0.801
Maximum $\varepsilon$ (°)	11.482	6.492
Standard deviation $\varepsilon$ (°)	0.733	0.208

from  $\langle 110 \rangle_\beta \parallel x_m$  and 4.0° misalignment from  $[001]_{\alpha''} \parallel z_m$ . The experimentally approached orientation relationship,  $\text{OR}^{\text{meas}}$ , is related to the theoretical orientation relationship,  $\text{OR}^{\text{theo}}$ , by the symmetry rotation matrix  $R^{\text{sym}}$ :

$$\text{OR}^{\text{meas}} = R^{\text{sym}} \text{OR}^{\text{theo}} = \begin{bmatrix} [100]_{\alpha''} \parallel [100]_\beta \\ [010]_{\alpha''} \parallel [01\bar{1}]_\beta \\ [001]_{\alpha''} \parallel [101]_\beta \end{bmatrix}$$

with

$$R^{\text{sym}} = \begin{bmatrix} 1 & 0 & 0 \\ 0 & 0 & 1 \\ 0 & -1 & 0 \end{bmatrix}.$$

According to the convention used by Chai *et al.* (2009), the theoretical orientation relationship  $\text{OR}^{\text{theo}}$  is defined as variant 1. The identified rotation matrix shows that the experimentally observed orientation variant is variant 2. The obtained crystal alignment can be used as an optimal starting point for preparing a TEM lamella for detailed characterization of the  $\beta$ - $\alpha''$  orientation relationship and the phase interface.

## 6. Discussion

### 6.1. Orientation accuracy and optimization robustness

From a computational point of view, the alignment procedure is based on a series of geometric and arithmetic operations and is therefore fully accurate to the degree of floating-point round-off errors. Errors in the overall sample alignment procedure are more likely to be introduced by the determination of the initial crystal orientation with EBSD, having an angular resolution of  $\sim 1^\circ$  (Dingley, 2004), sample misalignment and stage positioning accuracy. In the case of a TEM lamella lift out as demonstrated in Section 4, the transfer and reattachment of the lamella and the mounting of the TEM lift-out grid introduce further potential alignment errors.

Being a heuristic method, the genetic algorithm is sensitive to the initial population. The choice of a uniformly distributed initial population ensures similar starting conditions for each optimization problem, but the path towards successful optimization of alignment objectives is not reproducible and may sometimes even favour non-optimal solutions. The robustness

of the genetic algorithm depends on the implementation of suitable selection criteria, crossover and mutation functions and the correct proportion of elite, crossover and mutation children in a new generation. It can be further increased by choosing a larger population size, which may be computationally more expensive but could lead to faster convergence.

To evaluate the robustness of the genetic algorithm, the accumulated optimal fitness function value  $\varepsilon$ , *i.e.* the sum of the fitness function values of each objective, was statistically evaluated for 1000 executions of the *crystalAligner* program on the first application example in Section 4. The results are summarized in Table 3. The median optimal fitness function value was  $0.872^\circ$  with a standard deviation of  $0.733^\circ$ . Increasing the default population size from 50 to 100 led to a reduction in the median optimal fitness function value to  $0.816^\circ$  with a standard deviation of  $0.208^\circ$ .

### 6.2. Applications

The application examples presented in this paper demonstrate that the crystal alignment algorithm is well suited for preparing a TEM lamella for *in situ* nano-mechanical testing along a specified crystal direction under controlled diffraction conditions and for alignment of orientation-related crystals for characterization and analysis. In the case of TEM lamella preparation, control over the crystal orientation of the lamella is also of interest for high-resolution TEM imaging and for the investigation of anisotropic material properties, for instance by electron energy loss spectroscopy for characterization of optical (Skalwold *et al.*, 2015; Quirke & Lacy, 1939) and magnetic properties (Krishnan & Raman, 1927; Uyeda *et al.*, 1963). Crystal alignment in the SEM may be applied for ECCI imaging (Zaefferer & Elhami, 2014), micro-mechanical testing (Yu *et al.*, 2010) or residual stress measurement by micro-scale FIB and digital image correlation (Lunt & Korsunsky, 2015).

## 7. Conclusions

The computer program *crystalAligner* was developed for weighted constrained experimental alignment of one or two crystal directions with the coordinate system of a SEM. The program simulates the rotation and tilt of the microscope stage and uses a genetic algorithm to globally optimize the alignment of crystal directions with the microscope coordinate axes. The possibility of considering all equivalent crystal directions and the use of the heuristic global optimization algorithm enables satisfactory crystal alignment even for constrained stage rotations. In cases where no ideal alignment is obtainable, the optimal solution is found by weighting of conflicting objectives. Two application examples served to demonstrate the workflow, functionality and robustness of the freely available computer program.

### Acknowledgements

The author gratefully acknowledges the support of Umberto Maria Ciucani of the Technical University of Denmark and

Azdiar A. Gazder of the University of Wollongong for beta-testing the computer program.

### Funding information

The author acknowledges the Danish Council for Independent Research (grant No. DFF-8027-00009B) for financial support. This research used the FEI NanoLab G3 CX and JEOL JEM-2011 funded by the Australian Research Council (ARC) – Linkage, Infrastructure, Equipment and Facilities (LIEF) grant (grant Nos. LE160100063 and LE0237478, respectively) located at the UOW Electron Microscopy Centre.

### References

- Bachmann, F., Hielscher, R. & Schaeben, H. (2010). *Solid State Phenom.* **160**, 63–68.
- Baker, J. E. (1987). *Proceedings of the Second International Conference Genetic Algorithms and their Applications*, pp. 14–21. Cambridge: Taylor & Francis.
- Borrajó-Pelaez, R. & Hedström, P. (2018). *Crit. Rev. Solid State Mater. Sci.* **43**, 455–474.
- Bunge, H.-J. (1982). *Texture Analysis in Materials Science: Mathematical Methods*. Berlin: Butterworths.
- Chai, Y. W., Kim, H. Y., Hosoda, H. & Miyazaki, S. (2009). *Acta Mater.* **57**, 4054–4064.
- Clausen, B., Lorentzen, T. & Leffers, T. (1998). *Acta Mater.* **46**, 3087–3098.
- Dingley, D. (2004). *J. Microsc.* **213**, 214–224.
- Dölle, H. (1979). *J. Appl. Cryst.* **12**, 489–501.
- Engler, O. & Randle, V. (2010). *Introduction to Texture Analysis*. Boca Raton: CRC Press.
- Giannuzzi, L. A., Drown, J. L., Brown, S. R., Irwin, R. B. & Stevie, F. A. (1998). *Microsc. Res. Tech.* **41**, 285–290.
- Goldberg, D. E. (1989). *Genetic Algorithms in Search, Optimization and Machine Learning*. Boston: Addison-Wesley Longman Publishing.
- Gutierrez-Urrutia, I., Zaefferer, S. & Raabe, D. (2009). *Scr. Mater.* **61**, 737–740.
- Humphreys, F. J. (2001). *J. Mater. Sci.* **36**, 3833–3854.
- Kirchlechner, C., Toth, F., Rammerstorfer, F. G., Fischer, F. D. & Dehm, G. (2017). *Acta Mater.* **124**, 195–203.
- Kocks, U. F., Tomé, C. N., Wenk, C.-R. & Beaudoin, A. J. (2000). *Texture and Anisotropy. Preferred Orientations in Polycrystals and Their Effect on Material Properties*. Cambridge University Press.
- Krishnan, K. S. & Raman, C. V. (1927). *Proc. R. Soc. London Ser. A*, **115**, 549–554.
- Lunt, A. J. G. & Korsunsky, A. M. (2015). *Surf. Coatings Technol.* **283**, 373–388.
- Mansour, H., Guyon, J., Crimp, M. A., Gey, N., Beausir, B. & Maloufi, N. (2014). *Scr. Mater.* **84–85**, 11–14.
- MathWorks (2016a). *MATLAB 2016b* (9.1.0.441655). The MathWorks Inc., Natick, Massachusetts, USA.
- MathWorks (2016b). *MATLAB Global Optimization Toolbox* (R2016b). Version 7.5. The MathWorks Inc., Natick, Massachusetts, USA.
- MathWorks (2016c). *MATLAB Documentation, Global Optimization Toolbox, Genetic Algorithm* (R2016b). The MathWorks Inc., Natick, Massachusetts, USA.
- Miller, B. L. & Goldberg, D. E. (1995). *Complex Syst.* **9**, 193–212.
- Naseri, R., Mitchell, D. R. G., Savvakini, D. G., Nancarrow, M. J. B., Furuhashi, T., Saleh, A. A., Gazder, A. A. & Pereloma, E. V. (2019). *Mater. Sci. Eng. A*, **747**, 232–243.
- Niessen, F. (2019a). *CAM2FIB*, <https://github.com/frankNiessen/CAM2FIB>.

- Niessen, F. (2019b). *crystalAligner*, <https://github.com/frankNiessen/crystalAligner>.
- Niessen, F. & Nancarrow, M. J. B. (2019). *Nanotechnology*, **30**, 435301.
- Noyan, I. C. & Cohen, J. B. (1987). *Residual Stress – Measurement by Diffraction and Interpretation*. New York: Springer Science and Business Media.
- Oddershede, J., Wright, J. P., Beaudoin, A. & Winther, G. (2015). *Acta Mater.* **85**, 301–313.
- Oxford Instruments (2016). *Aztec 3.3*. Oxford Instruments, Abingdon, Oxfordshire, UK.
- Quirke, T. T. & Lacy, W. C. (1939). *Am. Mineral.* **24**, 705–724.
- Skalwold, E. A. & Bassett, W. A. (2015). *Double Trouble: Navigating Birefringence*. Chantilly: Mineralogical Society of America.
- Tseng, G.-H. & Huang, J.-J. (2011). *Multiple Attribute Decision Making – Methods and Applications*. London, New York: CRC Press/Taylor & Francis Group.
- Ungár, T., Dragomir, I., Révész, Á. & Borbély, A. (1999). *J. Appl. Cryst.* **32**, 992–1002.
- Uyeda, S., Fuller, M., Belshé, J. C. & Girdler, R. W. (1963). *J. Geophys. Res.* **68**, 279–291.
- Ye, J., Mishra, R. K., Pelton, A. R. & Minor, A. M. (2010). *Acta Mater.* **58**, 490–498.
- Yu, Q., Shan, Z. W., Li, J., Huang, X., Xiao, L., Sun, J. & Ma, E. (2010). *Nature*, **463**, 335–338.
- Zaefferer, S. (2000). *J. Appl. Cryst.* **33**, 10–25.
- Zaefferer, S. & Elhami, N. N. (2014). *Acta Mater.* **75**, 20–50.